MRA Visualization of Abnormal Tumor Vasculature in Genetically Engineered Mice

Lauren M. Brubaker[1], **Elizabeth Bullitt**[2], **Chaoying Yin**[3], **Terry Van Dyke**[4], and **Weili Lin**[1]

1 *Department of Radiology, Lineberger Comprehensive Cancer Center, University of North Carolina at Chapel Hill, Chapel Hill, NC, United States*

2 *Department of Surgery, Lineberger Comprehensive Cancer Center, University of North Carolina at Chapel Hill, Chapel Hill, NC, United States*

3 *Department of Biochemistry and Biophysics, Lineberger Comprehensive Cancer Center, University of North Carolina at Chapel Hill, Chapel Hill, NC, United States*

4 *Department of Genetics, Lineberger Comprehensive Cancer Center, University of North Carolina at Chapel Hill, Chapel Hill, NC, United States*

Abstract

Previous research on the vasculature of tumor-bearing animals has focused upon the microvasculature. Magnetic resonance angiography (MRA) offers a noninvasive, complementary approach that provides information about larger vessels. Quantitative analysis of MRA images of spontaneous preclinical tumor models has not been previously reported.

Eleven $TgT_{121};p53^{+/-}$ mice, which invariably develop choroid plexus carcinoma (CPC), and nine age-matched healthy controls were imaged using T1, T2, and a high-resolution 3D time-of-flight (TOF) MRA sequences at 3T. Tumors and vessels were segmented to determine tumor volume and vascular attributes, including number of terminal branches (TBC), vessel count (VC), and the average vessel radii (AVRAD) of MRA-visible vessels within the tumor. Differences in the vasculature between tumor-bearing animals and healthy controls were analyzed statistically. Although the spatial resolution of MRA prohibits visualization of capillaries, a high density of intra-tumor blood vessels was visualized in CPC mice. A significant increase in TBC and VC, but not AVRAD, was observed in CPCs when compared to normal controls. Both TBC and VC were highly correlated with tumor volume. This study represents the first MRA analysis of a spontaneous preclinical brain tumor model. Although the spatial resolution of MRA is less than histological analysis, MRA-obtained vascular attributes provide useful information with full brain coverage. We show that consistent tumor vasculature properties can be determined by MRA. Such methods are critical for developing preclinical therapeutic testing and will help guide the development of human brain tumor analyses.

Keywords

MR; Angiography; Angiogenesis; choroid plexus; genetically engineered mice; brain tumor

Introduction

A critical stage in the development of aggressive cancers is the establishment of a blood supply. Much research has been devoted to understanding this process using preclinical models that involve cell line transplantation such as xenografts. Furthermore, numerous clinical trials have been initiated to test the efficacy of angiogenesis inhibitors with limited success despite in spite of promising preclinical xenograft data [1–2]. In recent years, several mouse models of cancer have been established that develop tumors de novo based on genetic events engineered into the mouse, and in several cases the transition to angiogenesis has been established [3–11]. These models provide an opportunity to develop methods for in vivo imaging to characterize the properties of tumor vasculature to develop sensitive strategies for preclinical testing.

Previous efforts to characterize tumor vasculature in mouse brain tumor models relied on sacrificing the animals, thus prohibiting longitudinal studies of angiogenesis. Extensive efforts have been devoted to the development of approaches capable of revealing the unique features associated with tumor neoangiogenesis in vivo. Specifically, non-invasive approaches such as dynamic susceptibility contrast (DSC) magnetic resonance (MR) imaging have been utilized to depict regional vascular density, potentially useful in differentiating lesion pathology [12–19]. In addition, the continual monitoring of MR signal changes post-contrast can provide consistent vascular permeability measurements in animal and human subjects [19,20]. Both MR approaches offer insight into the microscopic physiological alterations associated with tumor vasculature. Little attention has been given to macroscopic vessels within these tumors, however.

High resolution MR angiography (MRA) offers a macroscopic view of the entire tumor vasculature. These parameters are likely to be of physiological importance by complementing MR perfusion and permeability studies. Indeed, in a recent blinded study of human tumor patients whose images were analyzed prior to lesion resection, a statistical analysis of the shapes of MRA-extracted blood vessels proved successful in separating benign from malignant disease in all cases [21].

The purposes of the current study are to determine whether tumor-associated vasculature can be visualized and extracted from the MRA images of tumor-bearing mice and, if so, to assess the properties quantitatively by which they differ from normal mice. The tumor model employed is a well-characterized, genetically engineered mouse model in which choroid plexus carcinoma (CPC) develops with 100% penetrance [6,7]. The histological characteristics of these tumors have also been well-studied [6,7] and mature tumors always exhibit marked angiogenesis.

This report describes the acquisition of high-resolution MR images, the extraction of blood vessels, the definition of tumors from the images of tumor-bearing animals, and the registration of images into a common coordinate system. For each tumor, we then statistically compare the number of terminal branches (TBC), the vessel count (VC), and the average vessel radius (AVRAD) to the means and standard deviations of the vasculature within the same anatomical region of the healthy controls. We conclude that tumor-associated vasculature can indeed be visualized and extracted successfully from the images of CPC-bearing mice.

Materials and Methods

Choroid Plexus Carcinoma (CPC) Mouse Model

T_gT_{121};$p53^{+/-}$ mice develop focally aggressive angiogenic CPC that is histologically detectable by 8 weeks and terminal by 12 weeks of age [7,22]. Often a single animal develops multiple focal tumors. Tumors are initiated by choroid plexus-specific expression of T_{121}, an

N-terminal fragment of SV40 large T antigen that binds and inactivates the tumor suppressor pRb and related proteins p107 and p130 [22]. T_{121} induces cell proliferation and p53-dependent apoptosis throughout the choroid plexus epithelium such that heterozygosity for a p53 null allele facilitates multi-focal tumor progression to CPC with complete p53 loss. Histological analyses show that the timing and penetrance of tumor development is highly reproducible [6]. CPC tumors are heavily vascular lesions, and thus provide an ideal tumor type in which to study the effect of anti-angiogenic agents in experimental animals.

A total of 20 mice were studied, including eleven $T_gT_{121};p53^{+/-}$ mice and nine age-matched control mice. Of the $T_gT_{121};p53^{+/-}$ animals, nine were terminal (10–11 weeks of age), while two were subterminal (8–9 weeks of age). All animal protocols were approved by the Institutional Care for Animal Use Committee.

Magnetic Resonance Imaging

All images were acquired on a Siemens 3T Allegra head only scanner (Siemens Medical Inc., Erlangen, Germany) with a maximum gradient strength of 40 mT/m and a slew rate of 400 mT/m/msec. A custom-made volume coil measuring 2.1 cm in diameter was utilized. Imaging sequences included a pre-contrast two-dimensional (2D) multi-slice T1 weighted sequence (T1W) ($30mm^2$ field of view (FOV), $0.1x0.1x1.0mm^3$ voxel size, repetition time (TR) 500ms, echo time (TE) 13ms, 4 averages, and acquisition time (TA) 8:46) and a 2D multi-slice T2 weighted sequence (T2W) ($30mm^2$ FOV, $0.1x0.1x1.0mm^3$ voxel size, TR 6990ms, TE 100ms, 4 averages, and TA 11:20). A high-resolution three-dimensional (3D) time-of-flight (TOF) MRA sequence was employed for acquiring MRA images ($30mm^2$ FOV, $0.1x0.1x0.1 mm^3$ voxel size, TR 53 msec, TE 8.8 msec, 2 averages, 256x256 resolution, and TA 23:11). All of the above imaging sequences were applied prior to the injection of a MR contrast agent (Gd-DTPA) Following an intraperitoneal injection of 0.5 mL Gadolinium contrast agent, post-contrast T1W images were acquired with identical parameters as above. Total acquisition time was approximately 1 hour.

Isoflurane, an inhalant anesthesia, was mixed with air and administered to animals at 2% induction and 1% maintenance through a nose cone. All mice were stereotactically immobilized prior to imaging.

Data analysis

All images were transferred to a PC for post-processing. Data analysis included vascular segmentation, lesion segmentation, image registration, derivation of vascular attributes, and statistical analysis.

Vessels were extracted from MRA images using a semi-automated, multi-scale method that proceeds from user-supplied seed points to automatically define the path of each vessel and to calculate the radius at each vessel point. Detailed descriptions of the vascular segmentation approaches are described in reference [23]. In short, the method models a vessel in three steps: (1) definition of a seed point on or near a vessel of interest; (2) automatic, dynamic-scale extraction of an image intensity ridge representing the vessel's central skeleton; and (3) automatic determination of vessel radius at each centerline point. The program's output defines each vessel as an ordered set of x, y, z points indicating the spatial position of that vessel's centerline with an associated radius at each point. For this report, we use the term "vessel" to indicate a single, unbranching structure. A single vessel might have one or more child branches, but the analyses described here count each child branch as an independent vessel.

Tumors were extracted from gadolinium-enhanced T1W images using a partially manual program that defines tumors via polygon drawing and filling on orthogonal cuts through an image volume [24].

All images were then registered via a normalized mutual-information based, affine registration into the coordinate system of one of the healthy mouse MRA studies [25]. Using a combination of forward and backward mapping, the same region of interest (the tumor boundary) could thus be mapped into the undeformed space of any animal's MRA. Registration of tumor-bearing mice into the healthy coordinate system was often difficult, as mice with large tumors possessed markedly bulging skulls without deformation of the jaw. In such cases, the brain was segmented and registration was performed upon the brain alone.

For each tumor, the surface was mapped into the tumor mouse's MRA and vessels were clipped to the tumor surface. Vascular attributes, as described below, were derived for the vessel segments contained by the region of interest (the volume defined by the tumor surface). This same region of interest was then mapped into the coordinate space of each healthy mouse, and the same vascular attributes were derived for each normal mouse. Note that although some vessels traversed the region of interest, analysis was only performed upon the vessel segments contained within the defined tumor region.

This paper considers three vessel attributes. The AVRAD was calculated by summing the radius at each centerline point and dividing by the number of vessel points. The VC was the number of vessels (including clipped vessels) within the confines of the tumor. Each branch counted as one vessel. The TBC was defined as the vessels lying entirely within the tumor (the terminal branches originate and end within the region of interest and no point in a terminal vessel branch lies outside the region). Hypervascular tumors induce the formation of new vessels within the tumor confines, and the TBC therefore provides an indirect measure of vessel sprouting. Figure 1 shows a region of interest (oval) and two vessels (thick lines) that traverse it. Three terminal branches are shown as narrow lines. The total vessel count would be 5 in this example. Traversing, entering, or exiting vessels are clipped to the tumor surface and analysis is performed only on the vessel segments lying within the confines of the region of interest. Finally, tumor volumes were calculated automatically by summing the number of voxels within the tumor and multiplying by the voxel size.

Statistical Analysis

In order to compare how vascular attributes differed between CPC and normal brain, we calculated the mean and standard deviation for each of the vascular attributes over the same anatomical location as each tumor in the 9 normal mice, allowing for the calculation of z-scores for each vascular attribute. In addition, linear regression analysis was utilized to determine the relation between AVRAD, VC, TBC, and lesion volume.

Results

Eleven T_gT_{121};$p53^{+/-}$ animals possessed a total of 15 tumors, each of which was analyzed independently. Three (mouse 01, 05 and 06, Table 1) of the nine terminal mice (mouse 00 to 09, Table 1) had more than one lesion. Gadolinium-enhanced images were not available or were of low quality in two animals; in these cases T2 images were used to define tumor margins.

The 3D TOF MRA images generated consistent high-resolution images of all mice in the study. Figure 2 provides an example of T1 (Fig. 2A), T2 (Fig. 2B), and MRA (Fig. 2C) and of the vessel trees (Fig. 2D) defined from a healthy mouse. Vessel trees are color-coded by circulatory group in this figure. Note that although the limits of MRA resolution preclude direct imaging of capillary beds, each of the major circulatory groups contains significant vascular detail.

Figure 3 provides an example of a subterminal mouse (mouse 07, Table 1) possessing multiple tiny tumors within a dilated ventricular system (arrow, Fig. 3a). In this case, the tumors were so multitudinous and small that no attempt was made to define the tumors individually, but the entire ventricular system was defined as a single region of interest for the later analysis of the vascular attributes.

The nine terminal mice each had one or more large tumors measuring approximately 4 mm in diameter, and located in the third, fourth and/or lateral ventricles. These larger tumors enhanced with gadolinium and were readily defined from contrast-enhanced T1 images. Figure 4 illustrates an example of a large tumor together with an associated histopathological slice. Note that small tumor nodules, less than 1 cubic mm in volume, can be seen on both the MR slice images and on the associated histopathological slice.

Results for AVRAD, VC, TBC and tumor volume for each tumor are summarized in Table 1. This table also provides the z-score values for AVRAD, VC, and TBC when compared to the age-matched normal controls at the same anatomical regions of the tumors. With the exception of a single very small mass (mouse 05; tumor 7), tumors displayed an increase in TBC and VC as compared to the matched anatomical region of control mice. This finding is consistent with the known hypervascularity associated with this particular tumor type. A lack of consistent regional difference in AVRAD is observed between tumor and healthy vessels, probably because tumor-associated neoangiogenesis produces an increase in vessels of a variety of sizes.

The interplay between lesion volume, TBC, and VC are shown in Figure 5, as compared between lesion volume and TBC (Fig. 5a), lesion volume and VC (Fig. 5b) and VC and TBC (Fig. 5c). A linear relationship exists between these three physiological parameters.

Discussion

Many evaluations of tumor angiogenesis using MRI have focused upon the utilization of perfusion imaging for estimating vascular density, with encouraging results reported by several groups [13–17]. Although still under investigation, dynamic contrast imaging may provide a promising approach as reported in both patient and animal studies [13–17]. However, disadvantages of perfusion imaging include confusion due to breakdown of the blood-brain barrier and omission of small foci of malignancy resulting from low spatial resolution.

This report takes an alternative, but complementary approach by describing visualization of the larger vessels directly discernable from MRA to investigate the feasibility of imaging murine tumors and vessels. As shown in Figures 3 and 4, abnormal vessels are clearly visible in both subterminal and terminal mice, suggesting that MRA may provide a reasonable means to monitor the progression of tumor angiogenesis in a preclinical tumor model.

As compared to healthy controls, a significant increase of TBC and VC were observed in CPC mice, which is in good agreement with previously described histological findings in this animal model [6]. Intuitively, one would expect a correlation between TBC and VC, since an increase in TBC will automatically produce an increase in vessel count. The TBC provides a count of short vessels contained entirely within a region of interest. Tumor-associated neoangiogenesis is likely to produce a statistically significant increase in TBC within a region of interest, since the tumor induces growth of new vessels within the tumor. Although an increase in TBC will also produce a rise in the total vessel count, the total vessel count is likely to be variable when a region of interest is mapped between a tumor subject and multiple healthy subjects since the mass effect of a tumor may displace vessels that would normally course within the region of interest. The two parameters TBC and VC are therefore related, but TBC is likely to provide a more reliable measure of tumor neoangiogenesis. In contrast, no significant differences were found in AVRAD between healthy animals and the tumor group, most likely due to tumor

neoangiogenesis involving both large and small vessels [26]. Both TBC and VC were linearly correlated with the lesion volume. This finding is in agreement with previous reports that describe homogeneity of this tumor as seen by histological section [6].

Our study is important for several reasons. First, to our knowledge, this report represents the first *in vivo* assessment of tumor vasculature based on MRA visible vessels in a well controlled genetic mouse brain tumor model. Second, all images were co-registered into a common coordinate system so that a direct comparison of the vasculature between CPC mice and normal controls at similar anatomical locations can be obtained. This ability is of importance since vessel distribution and shape is not uniform throughout the brain. Such registration will likely be helpful to follow tumor progression or response to treatment in individual animals over time.

Third, the vascular segmentation and analysis methods described provide automated, quantitative measures of vessel shape and density with statistical comparison to a database of healthy controls. Although the spatial resolution of MR images is not as high as that of histology, the quantitative parameters offered by our approach allow direct assessment of vascular morphology with coverage of the entire head in a noninvasive fashion.

Finally, tumor volume is calculated automatically. This ability is not only likely to prove helpful when following animals over time, but is clearly useful in enabling a direct comparison between several vascular attributes and lesion volume. Nevertheless, only post-contrast T1W images were used to define tumor margins. It is possible that combination of T1W and T2W images, particularly FLAIR sequences may further improve our ability to accurately define the margin of tumors althoug this is beyond the scope of our current study.

Although a spatial resolution of $0.1mm^3$ was achieved, capillaries cannot be visualized by MR and the experimentally derived vascular morphological parameters are only applicable for MRA visible vessels. The smallest vessels we were able to define had a diameter of 0.1 mm^3, as is compatible with the voxel size of the images acquired.

The method of registration employed was both affine and tissue based and may not be the optimal method of aligning images when the purpose is to compare vasculature between individuals. A deformable, vessel based registration method would be preferable. Others in our group are currently developing such an approach [22].

Future studies will focus on the following areas. First, as mentioned previously, many studies have focused on vascular density as measured by perfusion imaging. It would be of interest to compare vessel density measurements by perfusion imaging to the vessel density of the larger vessels imaged here. We have not performed perfusion imaging in this study because severe leakage of the blood brain barrier may confound estimates of vascular density. Nevertheless, an intravascular contrast agent such as AIM227 could potentially overcome this difficulty and provide an accurate estimate of vascular density. This study is currently in progress.

Second, the approach described in this report is applicable to longitudinal, non-invasive studies of individual animals. The ability to follow animals over time and to assess the vessel changes associated with malignancy in a non-invasive fashion will be of significant value to all investigators exploring the development and treatment of animal tumor models that closely mimic human tumors.

Finally, unlike perfusion imaging, which measures only vessel density, the definition of individual vessels from high-resolution MRA allows quantitative assessment of multiple measures of vessel shape. Several of these vessel attributes may be useful in the evaluation of disease [23,28,29]. The ability to define mouse tumor vessels individually as described in this

report will facilitate larger studies that can evaluate tumor neoangiogenesis not only on the basis of vessel density but also with the incorporation of other vessel attribute measures.

Conclusion

In summary, this report describes a set of methods useful for imaging brain tumors and, more uniquely, brain vasculature in the mouse. We describe results obtained in 9 healthy and 11 tumor-bearing animals, and conclude that high-resolution images can be obtained using a 3T scanner within a reasonable time frame. In addition, the ability to segment vessels and brain tumors allows a direct analysis of the vasculature in relation to the brain tumors in living animals. The ability to conduct repeated studies using MRA offers a valuable tool for directly monitoring the effectiveness of different antiangiogenic therapies without sacrificing animals.

References

1. Cao Y. Antiangiogenic cancer therapy. Semin Cancer Biol 2004;14:139–45. [PubMed: 15018898]

2. Gately S, Kerbel R. Therapeutic potential of selective cyclooxygenase-2 inhibitors in the management of tumor angiogenesis. Prog Exp Tumor Res 2003;37:179–92. [PubMed: 12795055]

3. Joyce JA, Baruch A, Chehade K, et al. Cathepsin cysteine proteases are effectors of invasive growth and angiogenesis during multistage tumorigenesis. Cancer Cell 2004;5:443–53. [PubMed: 15144952]

4. Radovanovic I, D'Angelo MG, Aguzzi A. Angiogenesis in transgenic models of multistep angiogenesis. Cancer Treat Res 2004;117:97–114. [PubMed: 15015554]

5. Huss WJ, Hanrahan CF, Barrios RJ, Simons JW, Greenberg NM. Angiogenesis and prostate cancer: identification of a molecular progression switch. Cancer Res 2001;61:2736–43. [PubMed: 11289156]

6. Lu X, Magrane G, Yin C, Louis DN, Gray J, Van Dyke T. Selective inactivation of p53 facilitatates mouse epithelial tumor progression without chromosomal instability. Mol Cell Bio 2001;17:6017–30. [PubMed: 11486039]

7. Symonds H, Krall L, Remington L, et al. Cell 1994;4:703–11. [PubMed: 8069917]

8. Smith-McCune K, Zhu YH, Hanahan D, Arbeit J. Cross-species comparison of angiogenesis during premalignant stages of squamous carcinogenesis in the human cervix and K14-HPV16 transgenic mice. Cancer Res 1997;57:1294–1300. [PubMed: 9102216]

9. Astrof S, Crowley D, George EL, et al. Direct test of potential roles of EIIIA and EIIIB alternatively spliced segments of fibronectin in physiological and tumor angiogenesis. Mol Cell Bio 2004;24:8662–70. [PubMed: 15367684]

10. Inoue M, Hafer JH, Ferrara N, Gerber HP, Hanahan D. VEGF-A has a critical, nonredundant role in angiogenic switching and pancreatic beta cell carcinogenesis. Cancer Cell 2002;1:193–202. [PubMed: 12086877]

11. Knies-Bamforth UE, Fox SB, Poulsom R, Evan GI, Harris AL. c-Myc interacts with hypoxia to induce angiogenesis in vivo by a vascular endothelial growth factor-dependent mechanism. Cancer Res 2004;64:6563–70. [PubMed: 15374969]

12. Kremer S, Grand S, Berger F, et al. Cerebral blood volume mapping by MR imaging in the initial evaluation of brain tumors. J Neuroradiol 2002;29:105–13. [PubMed: 12297732]

13. Principi M, Italiani M, Guiducci A, et al. Perfusion MRI in the evaluation of the relationship between tumour growth, necrosis and angiogenesis in glioblastomas and grade 1 meningiomas. Neuroradiology 2003;45:205–11. [PubMed: 12687302]

14. Shin JH, Lee HK, Kwun BD, et al. Using relative cerebral blood flow and volume to evaluate the histopathologic grade of cerebral gliomas: preliminary results. AJR Am J Roentgenol 2002;179:783–9. [PubMed: 12185064]

15. Law M, Cha S, Knopp EA, Johnson G, Arnett J, Litt AW. High-grade gliomas and solitary metastases: differentiation by using perfusion and proton spectroscopic MR imaging. Radiology 2002;222:715–21. [PubMed: 11867790]

16. Law M, Yang S, Wang H, et al. Glioma Grading: Sensitivity, specificity, and predictive values of perfusion MR imaging and proton MR spectroscopic imaging compared with conventional MR imaging. AJNR 2003;24:1989–98. [PubMed: 14625221]

17. Lee SJ, Kim JH, Kim YM, et al. Perfusion MR imaging in gliomas: comparison with histologic tumor grade. Korean J Radiol 2001;2:1–7. [PubMed: 11752962]

18. Cha S, Johnson G, Wadghiri YZ, et al. Dynamic, contrast-enhanced perfusion MRI in mouse gliomas: correlation with histopathology. Magn Reson Med 2003;49:848–55. [PubMed: 12704767]

19. Verhoye M, van der Sanden BP, Rijken PF, et al. Assessment of the neovascular permeability in glioma xenografts by dynamic T(1) MRI with Gadomer-17. Magn Reson Med 2002;47:305–13. [PubMed: 11810674]

20. Aronen HJ, Perkio J. Dynamic susceptibility contrast MRI of gliomas. Neuroimaging Clin N Am 2002;12:501–23. [PubMed: 12687908]

21. Bullitt E, Jung I, Muller K, et al. Determining malignancy of brain tumors by analysis of vessel shape. Lecture Notes in Computer Science 2004;3217:645–53.

22. Saenz Robles MT, Symonds H, Chen J, Van Dyke T. Induction versus progression of brain tumor development: differential functions for the pRB- and p53-targeting domains of simian virus 40 T antigen. Mol Cell Biol 1994;14:2686–98. [PubMed: 8139568]

23. Aylward S, Bullitt E. Initialization, noise, singularities and scale in height ridge traversal for tubular object centerline extraction. IEEE TMI 2002;21:61–75.

24. Prastawa M, Bullitt E, Moon N, Van Leemput K, Gerig G. Automatic brain tumor segmentation by subject specific modification of atlas priors. Acad Radiol 2003;10:1341–8. [PubMed: 14697002]

25. Rueckert D, Sonoda LI, Hates C, Hill DLG, Leach MO, Hawkes DJ. Non-rigid registration using free-form deformations: Application to breast MR images. IEEE Transactions on Medical Imaging 1999;18:712–21. [PubMed: 10534053]

26. Li CH, Shan S, Huang Q, et al. Initial stages of tumor cell-induced angiogenesis: evaluation via skin window chambers in rodent models. J Natl Cancer Inst 2000;92:143–7. [PubMed: 10639516]

27. Jomier J, Aylward S. Rigid and Deformable Vasculature-to-Image Registration: a Hierarchical Approach. Lecture Notes in Computer Science 2004;3216:821–8.

28. Bullitt E, Ewend M, Aylward S, et al. Abnormal vessel tortuosity as a marker of treatment response of malignant gliomas: Preliminary report. In press Technology in Cancer Research and Treatment.

29. Bullitt E, Gerig G, Pizer S, Aylward SR. Measuring tortuosity of the intracerebral vasculature from MRA images. IEEE-TMI 2003;22:1163–71.
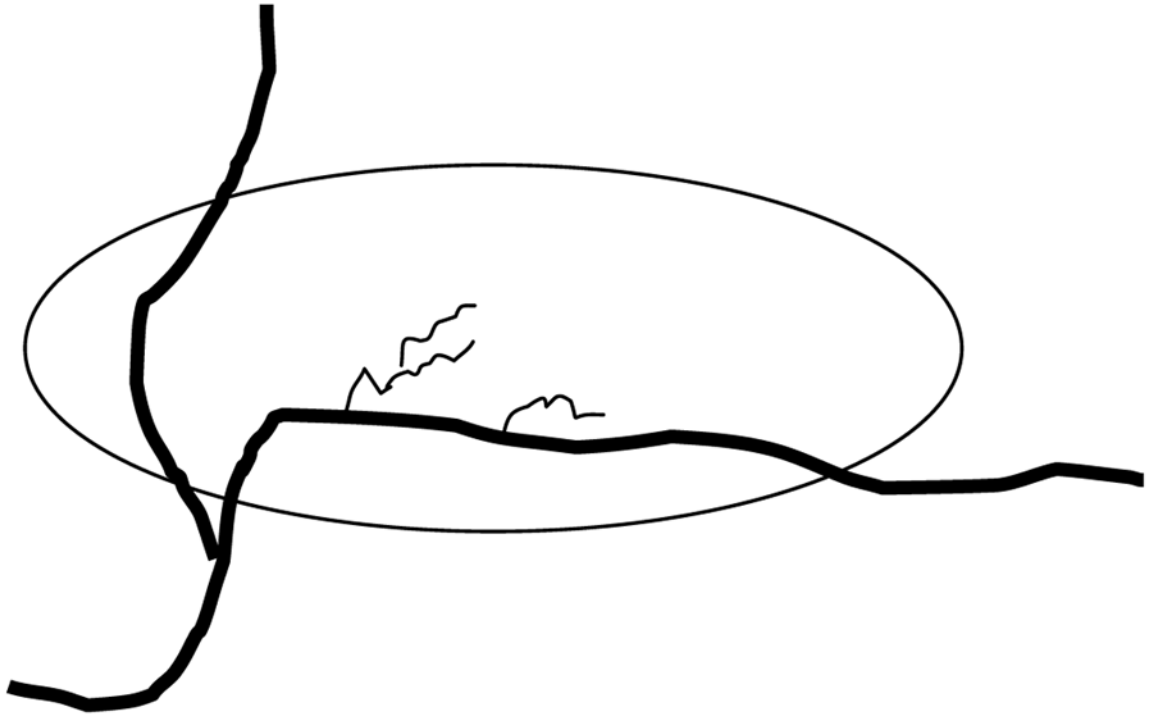
Fig. 1.
Diagram demonstrates an oval region of interest with two vessels (thick lines) traversing the region and three terminal branches (narrow lines). The total vessel count would be 5 in this example.
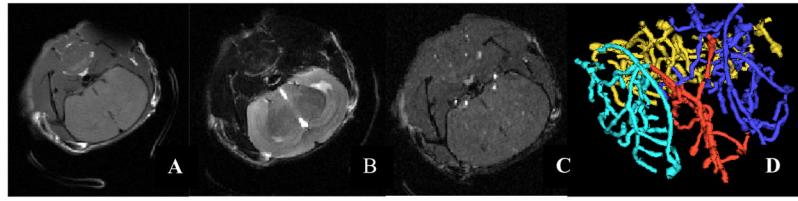
Fig. 2. Control Age-Matched Mouse
A: Pre-contrast T1 image, B: T2 image C: MRA D: corresponding vessel segmentation. For segmented vessels, blue = right middle cerebral group, cyan = left middle cerebral group, red = anterior cerebral group, gold = posterior cerebral group. The segmented vessels are shown from an AP point of view similar to that of the slice sections.
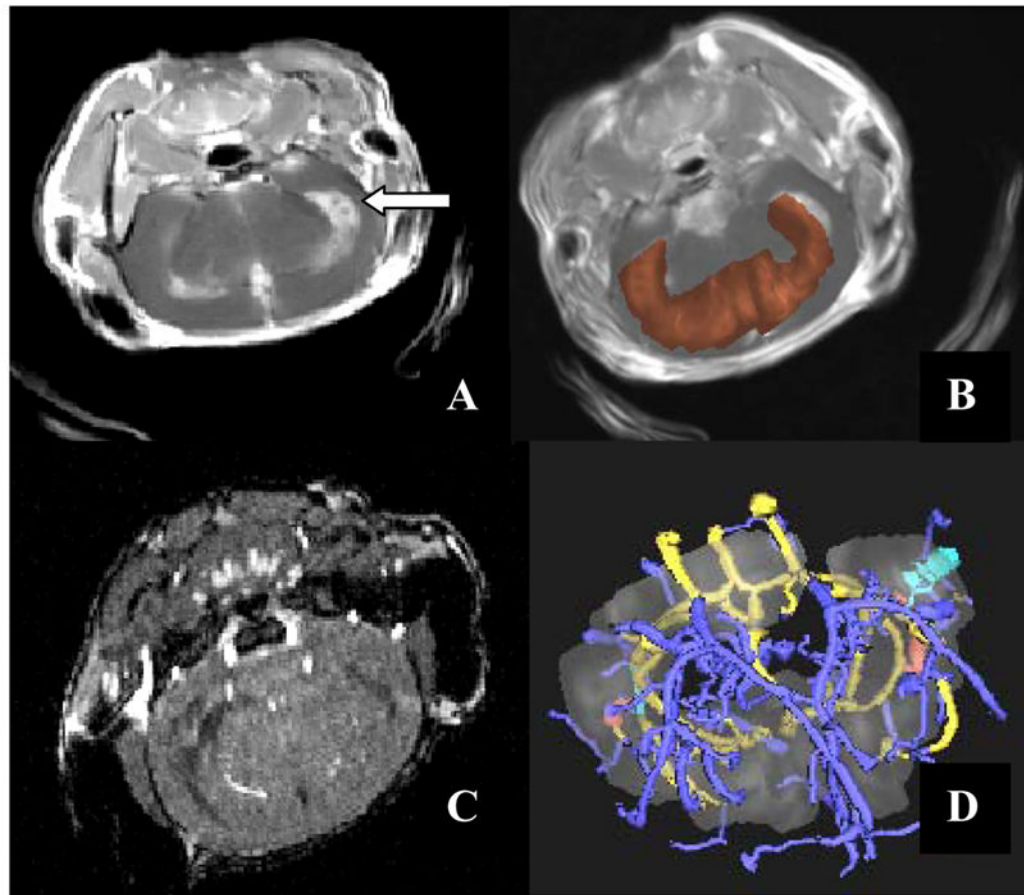
Fig. 3. Subterminal CPP Tumor Mouse
A: Post contrast T1 slice. Arrow points to a cluster of tiny tumors, B: 3D visualization of the extracted ventricular system with superimposition of the same slice seen in (A). C: MRA slice at the same level. D: 3D visualization of the segmented ventricular system (grey) shown at partial opacity together with the segmented vessels. Vessels are color coded relative to the ventricular surface such that blue = outside, gold = traverse, and red = inside. The 3D visualization is shown from an AP view.
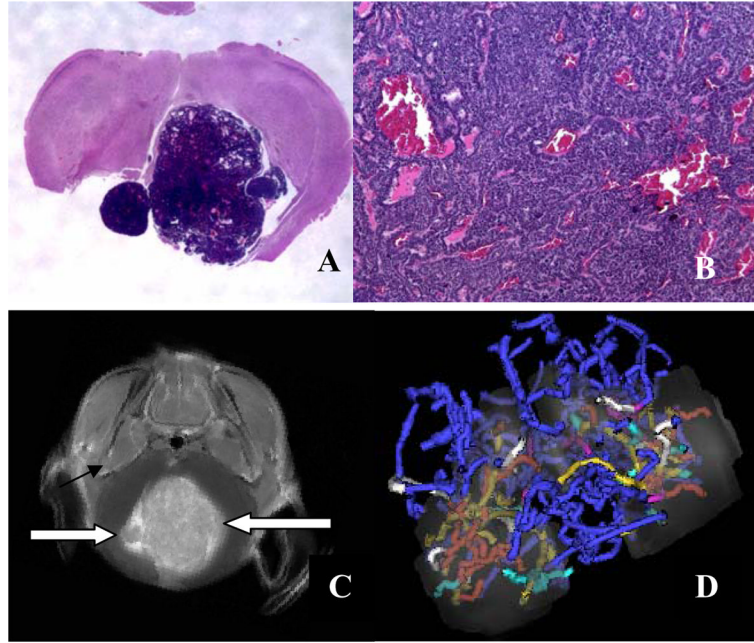
Fig. 4. Terminal CPP Tumor Mouse
A: Low-magnification histological section illustrating a large tumor within the third ventricle. Arrows point to small tumor nodules adjacent to the large tumor. B: Magnification of the same histological slice shown in A. Note the heavy vascularity of this tumor. C. Gadolinium-enhanced T1 slice at the corresponding level of the histological slice shown in A. Arrows point to the small tumor nodules. D: 3D visualization of the magnified segmented tumor (grey) drawn at partial opacity and with vessels color-coded relative to the tumor surface. Blue = outside, red = inside, gold = traverse, cyan = entering or exiting, white = traversing vessels with less than five vessel points within the tumor (excluded from analysis). There is marked neoangiogenesis, producing an increase in vessel number both within and surrounding the tumor. The tumor is very large, extending far beyond the confines of the mass shown in the single sections displayed in 4A-C. The 3D visualization is again shown from an AP view.
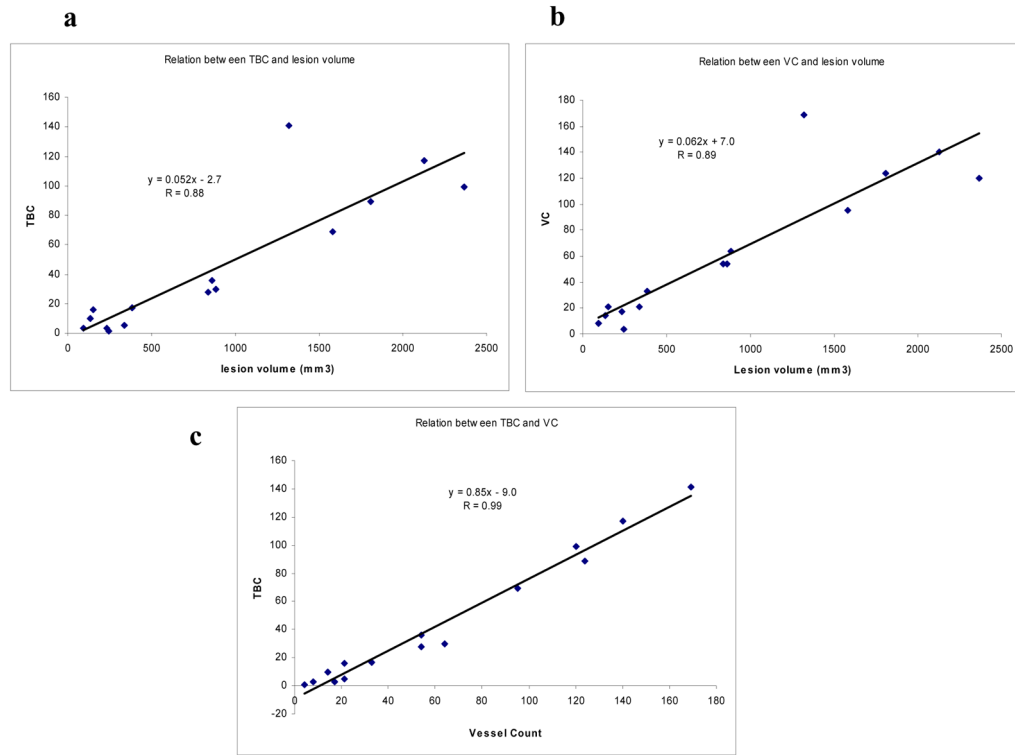
Fig. 5.
Correlation between TBC and lesion volume (a), VC and lesion volume (b), and TBC and VC (c), respectively. Note: Outlier data point due to difficultly in defining true tumor margins from lack of contrast enhanced T1 image

Table 1

Summary of AVRAD, TBC and TV.

Mouse	00	01A	01B	02	03	04	05A	05B	06A	06B	06C	07	09	10	11
Tumors	1	2	3	4	5	6	7	8	9	10	11	12	13	14	15
AVRAD (mm)	0.11	0.11	0.11	0.11	0.11	0.63	0.06	0.06	0.09	0.08	0.07	0.09	0.07	0.11	0.70
TBC	89	99	36	30	141	3	117	1	10	3	28	5	69	17	16
VC	124	120	54	64	169	17	140	4	14	8	54	21	95	33	21
TV (mm^3)	1806	2364	862	882	1321	234	2127	244	135	91	835	337	1581	383	152
Z-score VC	3.08	4.93	6.07	2	10.8	0.7	6.1	−1.1	7.4	2.6	2.6	1.04	0.6	3.04	0.5
Z-score AVR	1.3	0.9	1.0	1.0	1.0	−1.3	−1.9	−1.1	−0.7	−0.6	−1.7	0.0	−1.3	0.8	−1.8
Z-score TBC	4.5	5.6	8.4	2.9	12.9	0.5	8.4	−0.3	10.7	4.8	4.2	1.4	3.7	3.5	1

Average vessel radius (AVRAD), terminal branch count (TBC), vessel count (VC), tumor volume (TV), and associated Z-scores reported in above table.